

# Nanoscale

Accepted Manuscript



This is an *Accepted Manuscript*, which has been through the Royal Society of Chemistry peer review process and has been accepted for publication.

*Accepted Manuscripts* are published online shortly after acceptance, before technical editing, formatting and proof reading. Using this free service, authors can make their results available to the community, in citable form, before we publish the edited article. We will replace this *Accepted Manuscript* with the edited and formatted *Advance Article* as soon as it is available.

You can find more information about *Accepted Manuscripts* in the [Information for Authors](#).

Please note that technical editing may introduce minor changes to the text and/or graphics, which may alter content. The journal's standard [Terms & Conditions](#) and the [Ethical guidelines](#) still apply. In no event shall the Royal Society of Chemistry be held responsible for any errors or omissions in this *Accepted Manuscript* or any consequences arising from the use of any information it contains.

# Facile Large-Scale Synthesis of Brain-like Mesoporous Silica Nanocomposite via a Selective Etching Process

Yu Chen,<sup>a,b</sup> Qihua Wang<sup>\*a</sup> Tingmei Wang,<sup>a</sup>

<sup>a</sup> State Key Laboratory of Solid Lubrication, Lanzhou Institute of Chemical Physics, Chinese Academy of Sciences, Lanzhou, 730000, P. R. China.

<sup>b</sup> University of Chinese Academy of Sciences, Beijing, 100039, P. R. China

**Abstract:** The core-shell structured mesoporous silica nanomaterials (MSNs) are experiencing rapid development in many applications such as heterogeneous catalysis, bio-imaging and drug delivery wherein a large pore volume is desirable. We develop an one-pot method to large-scale synthesis of brain-like mesoporous silica nanocomposite based on the reasonably change of intrinsic nature of –Si-O-Si– framework of silica nanoparticles together with a selective etching strategy. The as-synthesized products show good monodispersion and large pore volume topped  $1.0 \text{ cm}^3 \text{ g}^{-1}$ . The novelty of this approach lies in the use of inorganic-organic hybrid layer to assist the creation of large-pore morphology on the outmost shell thereby promoting efficient mass transfer or storage. Importantly, the method is reliable and grams of products can be easily prepared. The morphology on the outmost silica shell can be controlled by simply adjusting VTES-to-TEOS molar ratios (VTES : triethoxyvinylsilane, TEOS: tetraethyl orthosilicate) as well as etching time. The as-synthesized products exhibit fluorescent performance by incorporating rhodamine B isothiocyanate (RITC) covalently into the inner silica walls, which provide potential application in bioimaging. We also demonstrate the applications of as-synthesized large-pore structured nanocomposites in drug delivery systems and stimuli-responsive nanoreactor for heterogeneous catalysis.

**Keywords:** *mesoporous silica, brain-like, core-shell, nanoreactor, drug delivery*

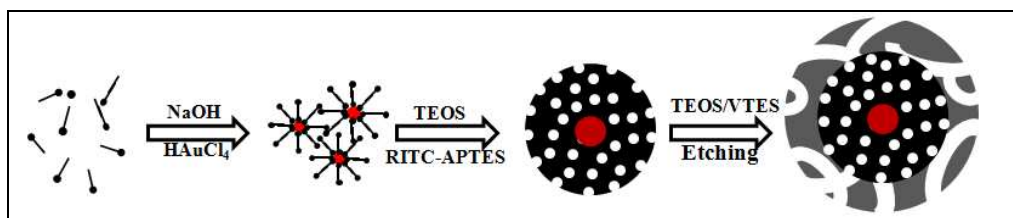
## 1. INTRODUCTION

After several decades of development, it is now possible to rationally design functional silicate materials on the nanometer scale by controlling their size, shape, composition, internal configuration, and surface properties.<sup>[1-9]</sup> In the research field of nanoparticulate materials, MSNs has attracted substantial attention during the past two decades due to their advantageous structural properties, such as biocompatibility, high internal surface area, colloidal stability and so on.<sup>[10-12]</sup> An important aspect about MSNs is that the core-shell structured MSNs with diverse properties could be achieved by encapsulating different materials.<sup>[13--21]</sup> These novel

structures make them widely used in many aspects such as separations, drug delivery, and bio-imaging wherein a large-pore MSNs (denoted as LPMSNs) is desirable. However, more porosity on the shell of a particle results in thin silica wall, which are prone to breakage or aggregation. Therefore, ultraporous mesostructured silica nanoparticles with good monodispersion is still challenge, especially for the core-shell structured MSNs with uniform size below 200 nm.

In addition, the pore diameters of contemporary MSNs synthesized by using cetyltrimethylammonium bromide (CTAB) as a pore-template can reach up to 3 nm. But LPMSNs (pore sizes > 3 nm) exhibit supremacy over smaller pore-MSNs with regard to storage, diffusivity, and penetration ability of large drug molecules or proteins. Several groups have reported the successful synthesis of LPMSNs that can be classified into two generally pathways.<sup>[22,23]</sup> One is to utilize the amphiphilic copolymers, surfactants with longer hydrophobic chains as well as inorganic nanoparticles, to act as pore-forming agent, while the second pathway is to utilize microemulsion media.<sup>[24-26]</sup> The above-mentioned LPMSNs provide a promising basis for wide-ranging applications in catalysis and drug delivery. However, these LPMSNs are either too large for application in life science or too complex to meet the demands of industrialization.<sup>[27,28]</sup> Moreover, these silicate structures are mostly of limited use because of the same component of core and shell materials. In view of these difficulties, it is highly valuable to develop a facile and large-scale synthetic approach for the fabrication of monodisperse multifunctional LPMSNs with tunable porosity and particle size, particularly the size of LPMSNs smaller than 200 nm.

In this work, we develop a facile and robust method for large-scale synthesis of brain-like structured Au@SiO<sub>2</sub> nanocomposites (denoted as LPASN) based on the reasonable change of intrinsic nature of –Si-O-Si– framework of silica shell together with a selective etching strategy. The morphology and particle sizes can be controlled by simply adjusting VTES-to-TEOS molar ratios as well as etching time. The pore size and pore volume can reach up to ~19 nm and ~1.3 cm<sup>3</sup>g<sup>-1</sup> via an etching process. We also demonstrate the multifunctional applications of LPASN for drug delivery and LPASN grafted with PNIPAM as stimuli-responsive nanoreactor for heterogeneous catalysis, respectively. Moreover, the as-synthesized LPASN exhibit fluorescent performance by incorporating rhodamine B isothiocyanate (RITC) covalently into the inner silica walls, which provide potential application in bioimaging. To the best of our knowledge, there are few reports of such a novel structured Au@SiO<sub>2</sub> nanocomposites, especially nanospheres with monodispersion and uniform size below 200 nm. More importantly, it is a reliable method for the fabrication of grams of products. The typical synthetic procedure for the LPASN includes three main steps, as shown in Scheme 1. After the *in situ* reduction of chloroauric acid by formaldehyde, the Au nanoparticles were stabilized by the surfactant CTAB in the alkaline aqueous solution. The electrostatic interactions between silicate oligomers hydrolysed from TEOS/APTES-RITC and CTAB-stabilized core materials lead to the formation of core-shell structured Au@CTAB/SiO<sub>2</sub>-RITC. After the addition of VTES/TEOS into the system, a hybrid outer layer was formed on the surface of Au@CTAB/SiO<sub>2</sub>-RITC by using the hydrolysis and co-condensation between TEOS and VTES. A dense and porous outermost shell can be more easily etched. Finally, brain-like structured LPASNs were obtained after selective-etching process.



**Scheme 1.** Schematic illustration of the preparation process for LPASN.

## 2. EXPERIMENTAL SECTION

**Chemicals.** All chemicals were analytical grade and used without further purification. Hexadecyl trimethyl ammonium bromide (CTAB), triethoxyvinylsilane (VTES), N-isopropylacrylamide (NIPAM), N,N-methylenebis (acrylamide) (MBA) and tetraethyl orthosilicate (TEOS) were purchased from Sigma. Potassium persulfate (KPS), (3-aminopropyl)triethoxysilane (APTES) were purchased from Aladdin. Gold chloride and sodium hydroxide were purchased from Sinopharm Chemical Reagent Co., Ltd. Ultrapure water ( $18.25 \text{ M}\Omega \text{ cm}^{-1}$ ) was obtained using a Nanopure system from Aquapro International Company LLC.

**Synthesis of RITC-APTES.** 10 mg of rhodamine B isothiocyanate (RITC) was reacted with  $44 \mu\text{L}$  of 3-aminopropyltriethoxysilane (APTES) (molar ratio of RITC:APTES = 1:10) in 0.75 mL of ethanol under dark conditions for 2 days. The prepared RITC-APTES stock solution was kept at  $4^\circ\text{C}$ .

**Synthesis of LPASN.** In a typical synthesis, 0.05 g Hexadecyl trimethyl ammonium bromide (CTAB) was dissolved in the deionized water (24 mL) containing NaOH (0.02 M). After stirring at  $80^\circ\text{C}$  for 20 min, formaldehyde solution (1.0M, 1 mL) and chloroauric acid aqueous solution (77.6 Mm, 1 mL) were separately added. Then, tetraethyl orthosilicate (TEOS) (0.15 g, 0.67 mM) was added with stirring and obtain Au@CTAB/SiO<sub>2</sub>. Ten minutes later, 20  $\mu\text{L}$  RITC-APTES was added. After stirring for a certain time, a mixture TEOS/VTES (molar ratios: 1:0.44/0.72/1.05) was added with vigorous stirring. The products were filtered after stirring for 24h/48h. To remove the surfactant, the as-synthesized products were dispersed in a solution of ethanol (120 mL) and ammonium nitrate (72 mg), and the mixture was heated at  $60^\circ\text{C}$  for 3 h.

### **Synthesis of LPASN-1 grafted PNIPAM**

The as-synthesized LPASN-1 were (35 mg) dispersed into 20 mL water/ 12mL ethanol by ultrasonication for 15 min, and then added into a 50 mL round-bottom flask with a magnetic stirrer, thermometer, nitrogen and Graham condenser. Then, NIPAM (50 mg) and cross linking agent MBA (5 mg) were added into the system. The dispersion was deoxygenated by a fine stream of nitrogen at room temperature for 30 min. The initiator KPS (25 mg) was added into the mixture and keep the polymerization process carrying out at  $75^\circ\text{C}$  for overnight. The LPASN-1 grafted PNIPAM was centrifuged and washed three times with ethanol.

**Synthesis of Yolk-shell Structures.** The synthesis for the yolk-shell structures was similar to the synthesis of LPASN, except the addition of APTES in the mixture containing TEOS/VTES (molar ratios: 1:0.72: 0.68).

### **Cytotoxicity Assay.**

The cytotoxicity of LPASN was investigated via standard MIT assays (MIT=3-(4,5-dimethylthiazol-2-yl)-2,5-diphenyltetrazolium bromide) using Hela cells. The cells

were initially seeded in 96-well plates at  $2 \times 10^4$  cells per well, and incubated in a standard growth medium for 24 h prior to exposure to the LPASN dispersion. The cells were then incubated with various concentrations of LPASN for 48 h. The absorbance of each well was measured at a wavelength of 570 nm by a microplate reader. The experimental results were calculated by the following formula: cell viability (%) =  $OD_{(SAMPLE)}/OD_{(CONTRAST)} \times 100$ , where  $OD_{(SAMPLE)}$  is the optical density of the treated cells measured, while  $OD_{(CONTRAST)}$  represents that of the untreated cells.

**Protein adsorption.** Protein adsorption experiments were carried out by contacting 100 mg of LPASN 4 with 100 mL of solution containing  $1 \text{ mg mL}^{-1}$  BSA in pH 4.7 and 50 mM acetate buffer. The solution were shaken at 150 rpm and  $25^\circ\text{C}$  for 6h. The amount of protein adsorbed was calculated by subtracting the amount found in the supernatant liquid after adsorption from the amount of protein present before the addition of the adsorbent LPASN, by UV absorption at 278 nm for BSA. The adsorbed amount of BSA was calculated according to the following equation:

$$q = V_0(C_0 - C) / W,$$

where  $q$  is the equilibrium adsorbed amount in the LPASN,  $C_0$  and  $C$  are the protein concentrations at initial and equilibrium solution, respectively,  $V_0$  the volume of the initial protein solution, and  $W$  is the weight of the adsorbent.

**Characterization.** X-ray diffraction (XRD) patterns were recorded using a Bruker D4 X-ray diffractometer with Ni-filtered Cu K $\alpha$  radiation (40 kV, 40 mA). Structural and morphological investigations of the products were performed using a Ultra-high resolution scanning electron microscope (HRSEM, SU8020) and transmission electron microscope (TEM, Tecnai-G2-F30). The fluorescence performance was recorded on a FL-920 T fluorescence spectrophotometer equipped with a 450 W Xe light source and double excitation monochromators. The nitrogen sorption experiments were performed at 77 K using a Micromeritics ASAP Tristar 3000 system. The samples were degassed at  $120^\circ\text{C}$  for 6 h using a vacuum line. The surface area and pore size were obtained by using Brunauer–Emmett–Teller (BET) and Barrett–Joyner–Halenda (BJH) methods, respectively. A Lambda 750 ultraviolet and visible (UV-vis) spectrophotometer was employed for the analysis of BAS adsorption and desorption.

### 3. RESULTS AND DISCUSSION

HRSEM images (Figure 1a) indicate the as-synthesized LPASN-1 consists of colloidal silica spheres of uniform size and the average size is 170 nm (Figure S. 1a). High magnification of these images reveals that the materials possess brain-like morphology on the shell (Figure 1b). Further structural characterization of as-synthesized silica nanospheres performed by transmission electron microscopy (TEM) reveals that the materials have a good dispersion and almost each core materials is encapsulated by a shell (Figure 1c). The efficiency of formation of core-shell structures can reach up to ninety-five percent. High-resolution transmission electron microscopy (HRTEM; Figure 1d) shows that LPASN-1 has a typical characteristic of double-shell structures, in which mesoporous pores disperse in the core and larger pores disperse in the outmost shells. The outmost shell appears porous and less homogeneous in transmission contrast, which attributed to partial and localized etching of silicate materials. The monodispersion of LPASN-1 was further demonstrated by high-angle annular dark-field scanning transmission electron microscopy (HAADF-STEM) (Figure 1e). Close inspection of these images further confirm the core-shell structured dual-mesoporous structures (Figure 1f). The composition and elemental distribution of LPASN-1 was mapped through energy dispersive X-ray spectroscopy (EDS) by displaying the

integrated intensity of silicon and gold signals as a function of the beam position when operating the transmission electron microscope in scanning mode. Mapping of elements indicates that both samples are composed of Si, O and Au.

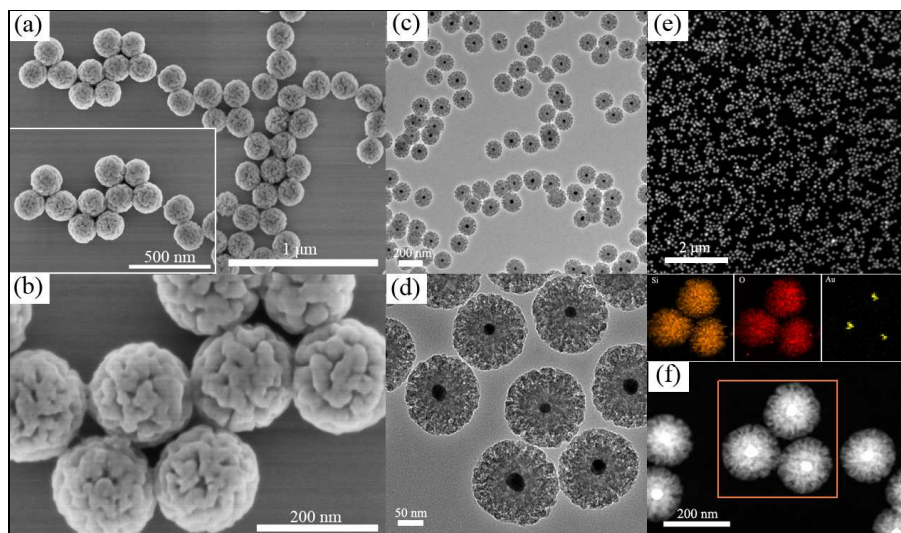


**Figure 1.** HRSEM (a, b), TEM (c, d), HAADF-STEM (e, f) images and their corresponding nanoscale elemental mappings of Si, O and Au (f) of LPASN-1.

The rhodamine B isothiocyanate (RITC) were incorporated covalently into the inner silica walls by treating these dyes with 3-aminopropyltriethoxysilane and carrying out a subsequent silica sol-gel reaction, thereby endowing the as-synthesized LPASN fluorescence property. The dye-derivatized Au@SiO<sub>2</sub> dispersed in water showed the typical emission of rhodamine B at 570 nm. The emission at 801 nm is attributed to Au nanoparticles (Figure 2a). LPASN with and without dye were well-dispersible in water. Under UV excitation, the dye-doped LPASN emitted colors, while there was almost no fluorescence from the LPASN without the dye (Figure 2b).

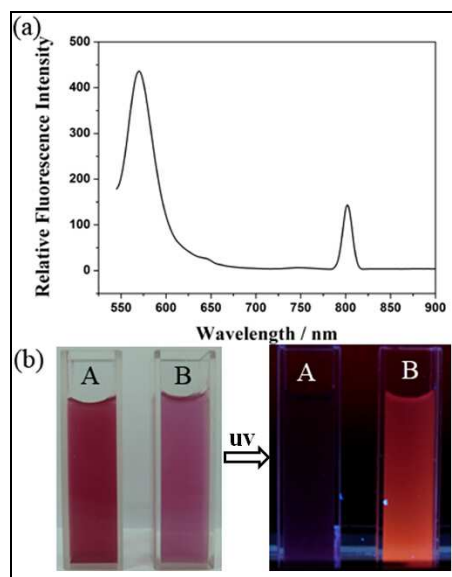


**Figure 2.** (a) Photoluminescence spectra of LPASN ( $\lambda_{\text{ex}}=520$  nm), (b) dispersion of LPASN

without (A) and with (B) dye functionalization in water under white light and UV light.

To study the effect of the organosilane on the silica morphology, VTES-to-TEOS molar ratios were varied, while other experimental parameters keep constant. When decreasing the amount of organosilane, a significantly increasing number of silicon atoms fully coordinated to nearest neighbours of other silicates would occur, thereby improving the ability of silica against alkaline etching. A relatively smooth surface was observed (denoted as LPASN-2) (Figure 3a), which is consistent with the results observed from the responding TEM images (Figure 3b). Meanwhile, the average particle size of LPASN-2 decrease from 170 nm to 130 nm. These results indicate that the VTES-to-TEOS molar ratios plays important role in adjusting the porous morphology. This was also evident when the synthesis of LPASN with an increasing amount of VTES was conducted. When increasing the amount of VTES, the  $-\text{Si-O-Si}-$  framework of the outer shell became less dense and more porous. Logically, less dense and more porous framework results in the larger particle size. However, in this case, a less dense and more porous shell is conducive to accelerate etching process of silica framework, thereby resulting in the structures collapsing in some extent. Therefore, in spite of adding more amount of VTES, the average particle size slightly decrease (Figure S. 1b). Different from the brain-like morphology, pore connectivity of LPASN-3 decrease (Figure 3d), while many independent larger pores formed (Figure 3c). Wide-angle XRD pattern of LPASN-2/LPASN-3/LPASN-4 was shown in Figure S2.

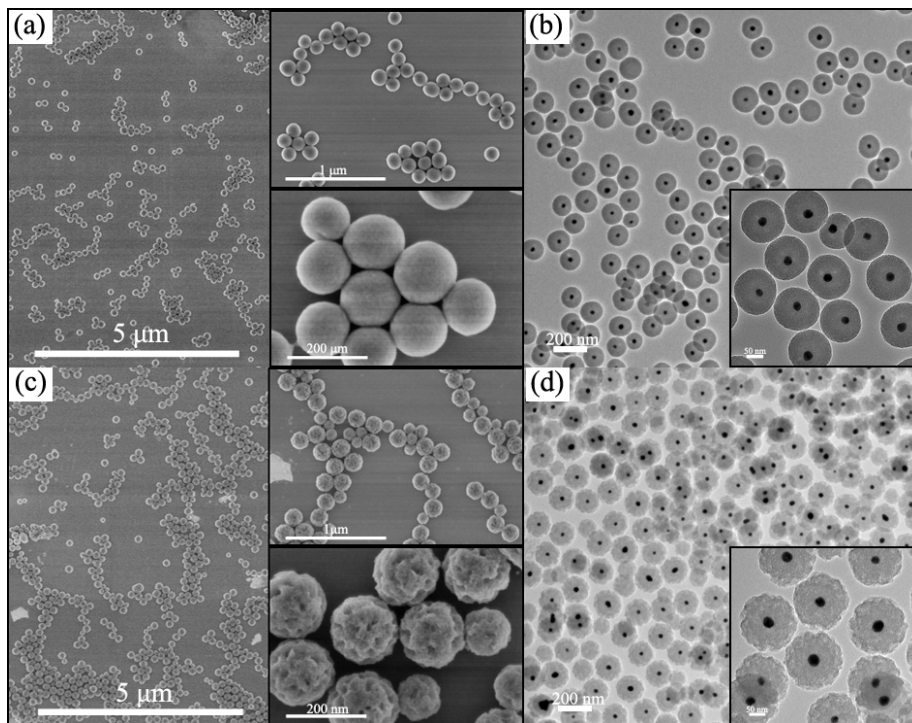


**Figure 3.** HRSEM and TEM images of the as-synthesized LPASN-2, LPASN-3 by adjusting VTES-to-TEOS molar ratios.

$\text{N}_2$  sorption analysis was performed to further demonstrate the structure of LPASN. As shown in Figure 4, the nitrogen sorption isotherms of the LPASN-1 show two major capillary condensation steps in the relative pressure ranges 0.1-0.3 and 0.75-0.98, respectively, indicating that two sets of

pores coexist in the materials. The average pore size at  $\sim 3.5$  nm and  $\sim 10$  nm can be observed from the corresponding distribution curve of LPASN-1, which is obtained by the Barrett-Joyner-Halenda (BJH) method. The pore distribution centered at  $\sim 3.5$  nm was mainly assigned to the CTAB template, while the pore distribution centered at  $\sim 10$  nm was assigned to the partial and localized etching of silicate materials, which result in a wide pore size distribution. In contrast, when decreasing or increasing VTES-to-TEOS molar ratios, obvious pore structures almost disappear. Note that the large distribution of pores above 20 nm belongs to inter particle voids between the packed LPASN. The porosity and average pore size can be controlled by adjusting VETS-to TEOS molar ratios, which is consistent with the results observed from their corresponding SEM and TEM images. Structure for more details was shown in Table 1.

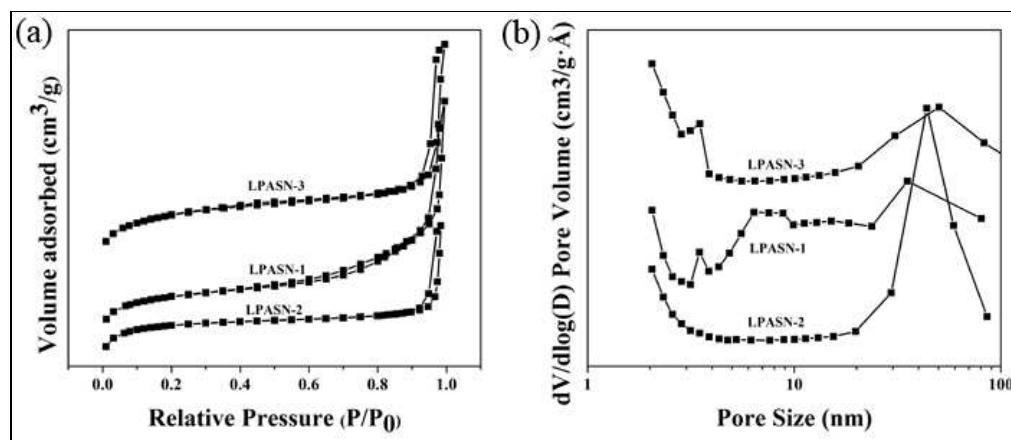


**Figure 4.**  $N_2$  physisorption isotherms of the as-synthesized LPASN-1/LPASN-2/LPASN-3 and their corresponding pore size distribution curves calculated by the BJH method.

**Table 1** Structure for more details.

Sample name	BET Surface Area ( $m^2 g^{-1}$ )	Pore Volume ( $cm^3 g^{-1}$ )	Pore Size (nm)
LPASN-1	473.8	0.56	12.1
LPASN-2	421.9	0.34	4.4
LPASN-3	460.3	0.38	7.3
LPASN-4	468.6	1.29	18.3

In addition to chemical stability, consistent pore structure and monodispersion, large-scale synthesis is also crucial for industrial application. The one-pot approach mentioned in this work does not require specific equipment as well as harsh conditions. Grams of LPASN can be easily prepared in a facile one-pot reaction. About  $\sim 3$  g of LPASN was prepared when the reaction system was expanded to 10 times (inset). Although a more porosity of outmost shell, the production still has good monodispersion as shown in Figure 5a. Note that, excepting for VTES-to-TEOS molar ratios, the morphology also has close connection with etching time. When extending the reaction time to 48 h, the materials became more porosity on the shell (Figure 5b). HRSEM images (Figure 5c) indicate the as-synthesized LPASN-4 consists of colloidal silica spheres with average size of  $\sim 140$  nm (Figure S. 1a) and the transformation from brain-like to flower-like morphology occurs. The pore size increases from  $\sim 11$  nm to  $\sim 19$  nm (Figure 5d).

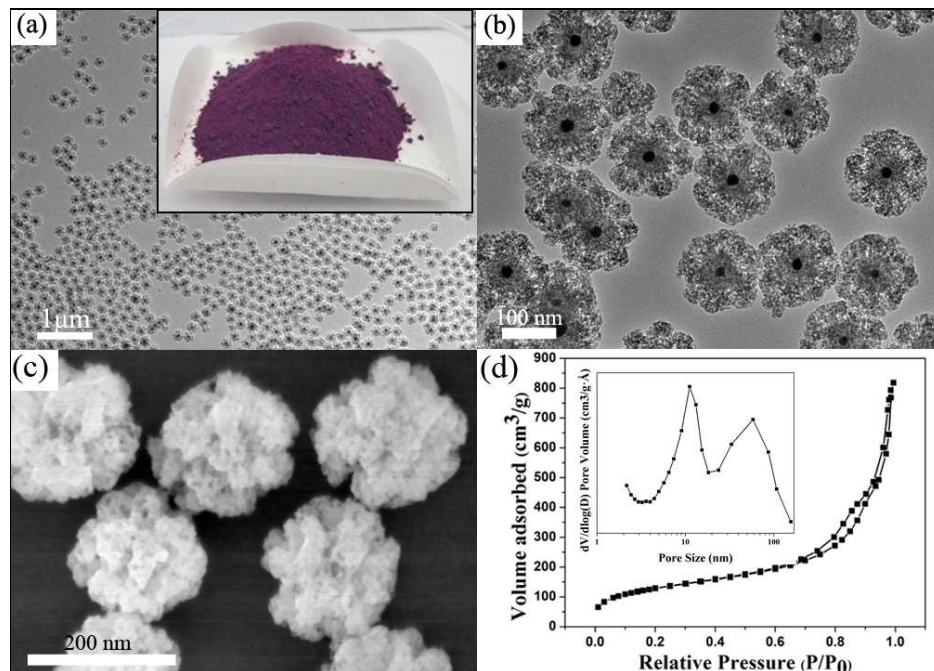
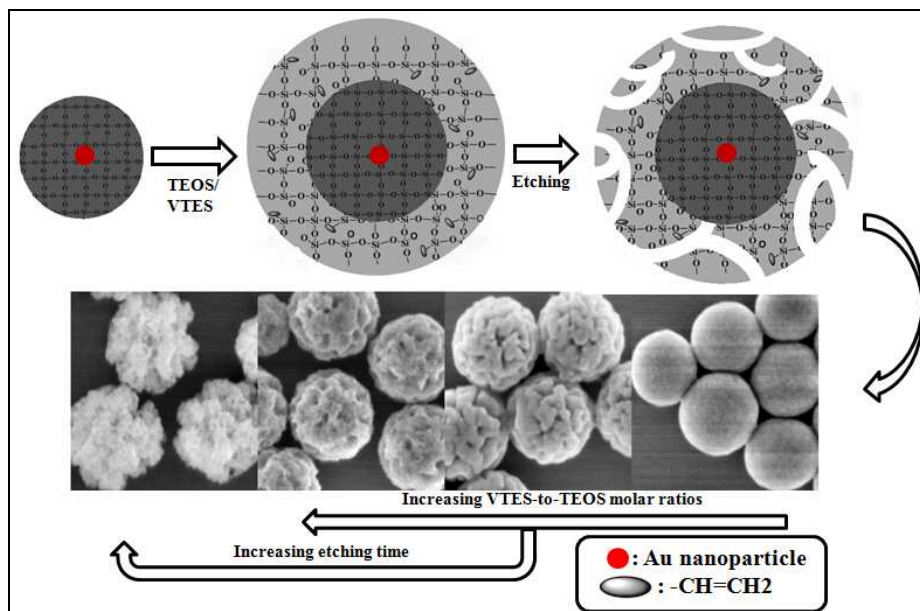


**Figure 5.** Low and high magnification TEM images of LPASN-4 and its corresponding photo of the as-synthesized LPASN-4 in a dish.

Based on the aforementioned results, a VTES-assisted selective etching mechanism was proposed to explain the formation of LPASN structures (Scheme 2). The electrostatic interactions between silicate oligomers hydrolysed from TEOS/APTES-RITC and CTAB-stabilized core materials lead to the formation of core-shell structured Au@CTAB/SiO<sub>2</sub>-RITC. After the addition of VTES/TEOS into the system, a hybrid outer layer was formed on the surface of Au@CTAB/SiO<sub>2</sub>-RITC by using the hydrolysis and co-condensation between TEOS and VTES. The outer shell was less dense and more porous because of the vinyl groups of VTES existing in silica framework. CTAB herein can not only act as a soft template to direct the formation of the mesoporous structures in the inner layer, but also stabilize the CTAB/SiO<sub>2</sub>-RITC inner shell against alkaline etching. Then, the sodium hydroxide, which was used in the synthesis, will preferentially etch the less dense and more porous VTES-rich silica shell, while the core almost remains intact. With increasing the concentration of VTES, a less dense and more porous outermost shell was obtained. However, such porous structures are conducive to accelerate etching process of silica framework, thereby resulting in the structures collapsing in some extent. Therefore, the numbers of vinyl groups existing in silica framework determine the ability of outer silica shell against alkaline etching, thereby obtaining different morphology (LPASN-1/LPASN-2/LPASN-3). In addition, as etching time increasing, some pores will merge into a large one resulting in a more rough morphology (LPASN-4). Therefore, the morphology has close connection with the VTES-to-TEOS molar ratios as well as etching time.



**Scheme 2.** The illustrate mechanism and their responding morphology at different VTES-to-TEOS molar ratios and etching time.

The choice of VTES as an organic precursor to assisted coassembly of inorganic-organic shell is the key to the successful synthesis of LPASN. In our previous report,<sup>[29]</sup> the CTAB/SiO<sub>2</sub> layer transform into a hollow cavity when adding APTES into the reaction system. When choosing APTES as organic precursor, the role of CTAB for stabilizing the silicate against alkaline etching was broken because of the electrostatic interactions between APTES and CTAB. On the other hand, the long hydrophobic chain  $-(\text{CH}_2)_3-$  existing in the silica shell can protect the silicate materials against the alkaline etching. In a word, the less dense and more porous part can be reasonably designed by choosing different organic precursor thereby deciding which part is preferentially etched. To confirm this, we replace TEOS/VTES with TEOS/VTES/APTES in the reaction system. APTES is more acidic and lower in concentration than the hydrolyzed TEOS in the mixture. Consequently, APTES/VTES should be consumed before TEOS. The less dense and more porous part is the middle layer via the hydrolysis and condensation of VTES/APTES and part of TEOS, which is preferentially etched by alkaline. Meanwhile, APTES oligomers reassembling into the outmost silica shell can protect the outmost layer against the alkaline etching. As a result, a novel yolk-shell structure was obtained as shown in Figure 6.

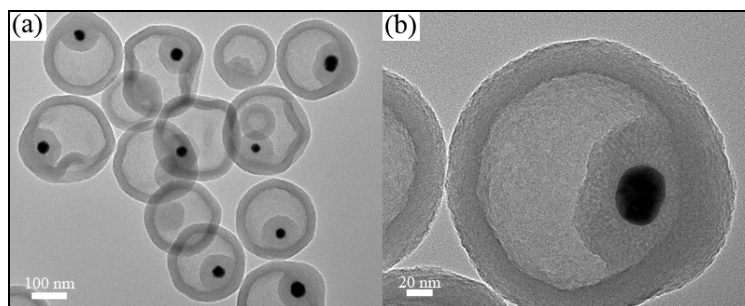


**Figure 6.** Low and high magnification TEM images of novel yolk-shell structures.

Cell viability by the MIT assay (MIT=3-(4,5-dimethylthiazol-2-yl)-2,5-diphenyltetrazolium bromide) revealed that the as-synthesized LPASN-1 do not show significant cytotoxicity against the HeLa cells (Figure 7a). More than 72% of the cells are still viable by the presence of LPASN-1 up to a concentration of  $200\mu\text{g} \cdot \text{mL}^{-1}$ . The results indicate that such a large-pore structured silica nanocomposite has good cytocompatibility as a drug carrier. As we known, CTAB as a general pore-template play important role in fabricating mesoporous silica materials. However, the pore diameters of contemporary MSNs synthesized by using CTAB as a pore –template can reach up to  $\sim 3$  nm. They exhibit considerable resistance of diffusion especially in the case of long transportation distance due to pore size limitation, which may limit their practical applications involving in large molecule transportation, such as protein enrichment. Herein, we demonstrate that the as-synthesized LPASN can promote efficient mass transfer or storage. The results of the protein adsorption of the LPASN are shown in Fig. 7b. For adsorption measurements, Ph 4.7 (near the pI of BSA) was chosen because the adsorption capacity can be maximized near the pI. Comparatively, LPASN 1 exhibits a low adsorption capacity of BSA due to its low BET surface area. On the hand, LPASN-4 reached adsorption equilibrium more quickly. The dimensions of the BSA molecule are reported to be  $40 \times 40 \times 140 \text{ \AA}$ . Since the largest dimension of BSA is close to the average pore size of LPASN-1, the large amount adsorbed in the original age is expected to be located on the external surface of LPASN or at the pore mouths.

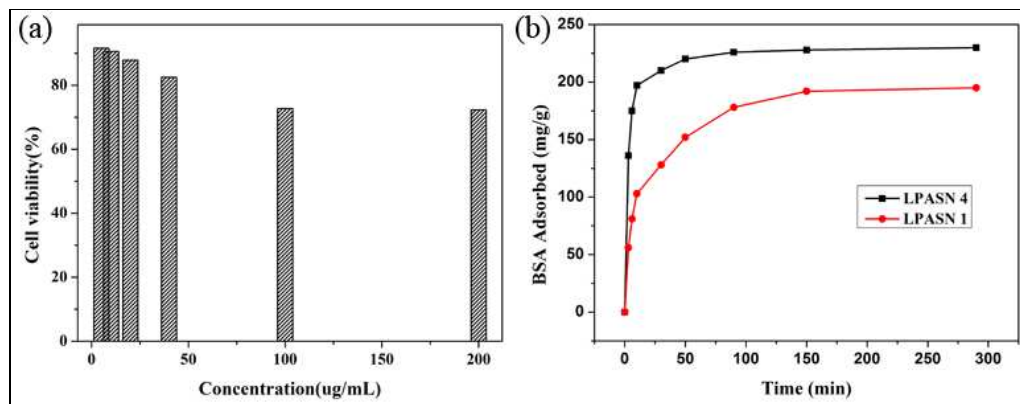


**Figure 7.** BSA adsorption curves of LPASN 4 and LPASN 1.

According to etching process, vinyl groups existing in the organic-inorganic hybrid layer will be preferentially etched thereby exposing a large number of vinyl groups on the surface of LPASN. Herein, we fabricate a thermo-responsive nonreactor by grafting LPASN with thermo-responsive polymer Poly(N-isopropyl acrylamide) (PNIPAM). FTIR spectroscopy was used to characterize the functional groups of the as-synthesized materials ( Figure 8a ). Bands located at  $1400$ ,  $1101$ ,  $953$  and  $802 \text{ cm}^{-1}$  are associated with the C-H bending vibration in unhydrolyzed OEt groups, the Si-O-Si asymmetric bond stretching vibration, the Si-OH stretching vibration, and the network Si-O-Si symmetric bond stretching vibration, respectively. Bands located at  $1600 \text{ cm}^{-1}$  attributed to the vinyl groups in VTES. The vinyl groups in LPASN greatly facilitate their practical application. After grafting PNIPAM, two characteristic peaks for PNIPAM at  $1650$  (amide stretch) and  $1553 \text{ cm}^{-1}$  (N-H stretch) appear in the LPASN-PNIPAM but not in LPASN. After calcinations at  $550 \text{ }^\circ\text{C}$ , the intensity of the bands related to vinyl groups, C-H bending vibration and Si-OH stretching vibration disappear or become indistinguishable, indicating that the removal of

organosilane and completely hydrolysis. The TEM images of PNIPAM-grafted LPASN-1 (denoted as LPASN-PNIPAM) as shown in Figure 8 b. The optical transmittance of LPASN-PNIPAM dispersed in aqueous solution can be controlled by temperature (Figure 5a, inset). The nanocomposite can be used as a thermo-responsive nanoreactor with controlled reaction rate. We used a well-known model reaction, where p-nitrophenol was reduced to p-aminophenol using  $\text{NaBH}_4$  as the reductant (Figure 8c). The reaction rate at different reaction temperature (15 °C / 33 °C / 50 °C) were compared (Figure 8d). The reaction rate at 15 °C and 50 °C were faster than 33 °C. The reasons were revealed in some reported literatures.<sup>[30]</sup> When the temperature higher than the lower critical solution temperature ( LCST ) of PNIPAM, the PNIPAM networks shrinks markedly with an increase in temperature thereby slowing down of the diffusion of reactants in and out the nonreactors. This change will in turn lower the rate of the reaction catalyzed by the Au nanoparticles encapsulated in LPASN-1. However, with a further increase in the temperature, thermal activity became the key factor that affecting the reaction rate. The catalytic properties of LPASN-PNIPAM for more details at different temperature were shown in Figure S3.

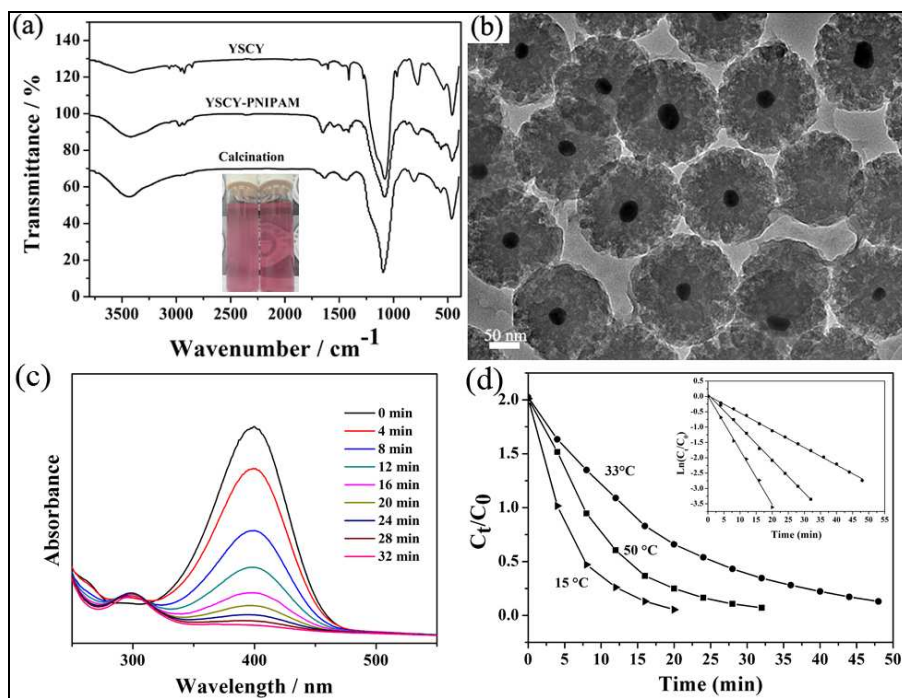


**Figure 8.** FTIR spectroscopy of LPASN, LPASN-PNIPAM and the products after calcinations at 550 °C (a); the inset shows the optical transmittance of LPASN-PNIPAM dispersed in aqueous solution. TEM images of LPASN-PNIPAM (b). UV-vis spectra showing the gradual reduction of 4-NP over LPASN-PNIPAM at 50 °C (c) and the plots of  $C_t/C_0$  versus the time at different temperature, where  $C_t$  is the concentration at time  $t$  and  $C_0$  is the initial concentration ( $\ln(C_t/C_0)$ ) (d).

In summary, we have developed a facile and reliable VTES-assisted selective etching strategy to fabricate monodisperse brain-like LPASN with uniform size below 200 nm. The porosity of shell can be controlled by adjusting VTES-to-TEOS molar ratios as well as etching time. The pore size and pore volume can reach up to  $\sim 19$  nm and  $\sim 1.3 \text{ cm}^3 \text{ g}^{-1}$  via an etching process that facilitate the adsorption of protein. Moreover, this strategy introduces vinyl groups on

the surface of the LPASN, which greatly facilitate their practical application in grafting PNIPAM for thermal-responsive nanoreactor. The fluorescence properties provide their potential applications in bio-imaging. This method may provide a general strategy to synthesize large-pore structured silica nanocomposite, which provide opportunities to yield a variety of applications, such as confined nanoreactor, drug delivery systems as well bio-imaging.

## ASSOCIATED CONTENT

### Supporting Information

The average particle size distribution of LPASN-1, LPASN-2 and LPASN-3; Wide-angle XRD pattern of LPASN-2/LPASN-3/LPASN-4; The catalytic properties of LPASN-PNIPAM at different temperature (15°C and 33 °C).

## AUTHOR INFORMATION

### Corresponding Author

\*E-mail: wangqh@licp.cas.cn. Fax: +86-0931-4968180.

### Notes

The authors declare no competing financial interest.

## Acknowledgements

We greatly appreciate financial support from the National Basic Research Program of China (973 Program, Grant No. 2015CB057502). Besides, the authors acknowledge Dr. Fan zengjie of Lanzhou University for in vitro cytotoxicity measurement.

## Reference

- (1) Y. Wan, D. Zhao, On the controllable soft-templating approach to mesoporous silicates, *Chem. Rev.*, 2007, **107** (7), 2821-2860.
- (2) C. T. Kresge, M. E. Leonowicz, W. J. Roth, J. C. Vartuli, J. S. Beck, Ordered mesoporous molecular-sieves synthesized by a liquid-crystal template mechanism, *Nature*, 1992, **359** (6397), 710-712.
- (3) M. E. Davis, Ordered porous materials for emerging applications, *Nature*, 2002, **417** (6891), 813-821.
- (4) H. Minakuchi, K. Nakanishi, N. Soga, N. Ishizuka, N. Tanaka, Octadecylsilylated porous silica rods as separation media for reversed-phase liquid chromatography, *Anal. Chem.*, 1996, **68** (19), 3498-3501.
- (5) H. Yang, Q. Lu, F. Gao, Q. Shi, Y. Yan, F. Zhang, S. Xie, B. Tu, D. Zhao, One-step synthesis of highly ordered mesoporous silica monoliths with metal oxide nanocrystals in their channels, *Adv. Funct. Mater.*, 2005, **15** (8), 1377-1384.
- (6) J. S. Beck, J. C. Vartuli, W. J. Roth, M. E. Leonowicz, C. T. Kresge, K. D. Schmitt, C. T. W. Chu, D. H. Olson, E. W. Sheppard, A new family of mesoporous molecular-sieves prepared with liquid-crystal template, *J. Am. Chem. Soc.*, 1992, **114** (27), 10834-10843.
- (7) J. Wei, Q. Yue, Z. Sun, Y. Deng, D. Zhao, Synthesis of Dual-Mesoporous Silica Using Non-Ionic Diblock Copolymer and Cationic Surfactant as Co-Templates, *Angew. Chem.*, 2012, **51** (25), 6149-6153.
- (8) C. Argyo, V. Weiss, C. Bräuchle, T. Bein, Multifunctional Mesoporous Silica Nanoparticles as a

- Universal Platform for Drug Delivery, *Chem. Mater.*, 2014, **26** (1), 435-451.
- (9) D. Chen, L. Li, F. Tang, S. Qi, Facile and Scalable Synthesis of Tailored Silica "Nanorattle" Structures, *Adv. Mater.*, 2009, **21** (37), 3804-3807.
- (10) Q. Zhang, W. Wang, J. Goebel, Y. Yin, Self-templated synthesis of hollow nanostructures, *Nano Today*, 2009, **4** (6), 494-507.
- (11) R. Ghosh Chaudhuri, S. Paria, Core/shell nanoparticles: classes, properties, synthesis mechanisms, characterization, and applications, *Chem. Rev.*, 2012, **112** (4), 2373-2433.
- (12) Y. J. Wong, L. F. Zhu, W. S. Teo, Y. W. Tan, Y. H. Yang, C. Wang, H. Y. Chen, Revisiting the Stober Method: in homogeneity in silica shells, *J. Am. Chem. Soc.*, 2011, **133** (30), 11422-11425.
- (13) X.-J. Wu, D. Xu, Soft template synthesis of yolk/silica shell particles, *Adv. Mater.*, 2010, **22** (13), 1516-1520.
- (14) J. Liu, S. Z. Qiao, S. Budi Hartono, G. Q. Lu, Monodisperse yolk-shell nanoparticles with a hierarchical porous structure for delivery vehicles and nanoreactors, *Angew. Chem.*, 2010, **49** (29), 4981-4985.
- (15) J. Lee, J. C. Park, H. Song, A nanoreactor framework of a Au@SiO<sub>2</sub> yolk/shell structure for catalytic reduction of p-nitrophenol, *Adv. Mater.*, 2008, **20** (8), 1523.
- (16) X. L. Fang, Z. H. Liu, M. F. Hsieh, M. Chen, P. X. Liu, C. Chen, N. F. Zheng, Hollow mesoporous aluminosilica spheres with perpendicular pore channels as catalytic nanoreactors, *ACS Nano*, 2012, **6** (5), 4434-4444.
- (17) Y. Chen, H. R. Chen, L. M. Guo, Q. J. He, F. Chen, J. Zhou, J. W. Feng, J. L. Shi, Hollow/Rattle-Type Mesoporous Nanostructures by a Structural Difference-Based Selective Etching Strategy, *ACS Nano*, 2010, **4** (1), 529-539.
- (18) X. J. Wu, D. S. Xu, Formation of yolk/SiO<sub>2</sub> shell structures using surfactant mixtures as template, *J. Am. Chem. Soc.*, 2009, **131** (8), 2774.
- (19) T. Zhang, J. Ge, Y. Hu, Q. Zhang, S. Aloni, Y. Yin, Formation of hollow silica colloids through a spontaneous dissolution-regrowth process, *Angew. Chem.*, 2008, **47** (31), 5806-5811.
- (20) Y. Chen, Q. Wang, T. Wang, Fabrication of thermally stable and active bimetallic Au-Ag nanoparticles stabilized on inner wall of mesoporous silica shell, *Dalton. Trans.*, 2013, **42** (38), 13940-13947.
- (21) L. Han, H. Wei, B. Tu, D. Zhao, A facile one-pot synthesis of uniform core-shell silver nanoparticle@mesoporous silica nanospheres, *Chem. Commun.*, 2011, **47** (30), 8536-8538.
- (22) K. Zhang, L. L. Xu, J. G. Jiang, N. Calin, K. F. Lam, S. J. Zhang, H. H. Wu, G. D. Wu, B. Albel, L. Bonneviot, P. Wu, Facile large-scale synthesis of monodisperse mesoporous silica nanospheres with tunable pore structure, *J. Am. Chem. Soc.*, 2013, **135** (7), 2427-2430.
- (23) V. Polshettiwar, D. Cha, X. Zhang, J. M. Basset, High-surface-area silica nanospheres (KCC-1) with a fibrous morphology, *Angew. Chem.*, 2010, **49** (50), 9652-9656.
- (24) J. Lu, M. Liong, Z. Li, J. I. Zink, F. Tamanoi, Biocompatibility, Biodistribution, and drug-delivery efficiency of mesoporous silica nanoparticles for cancer therapy in animals, *Small*, 2010, **6** (16), 1794-1805.
- (25) Q. He, Z. Zhang, F. Gao, Y. Li, J. Shi, In vivobiodistribution and urinary excretion of mesoporous silica nanoparticles: effects of particle size and PEGylation, *Small*, 2011, **7** (2), 271-280.
- (26) S. M. Egger, K. R. Hurley, A. Datt, G. Swindlehurst, C. L. Haynes, Ultraporous mesostructured silica nanoparticles, *Chem. Mater.*, 2015, **27** (9), 3193-3196.
- (27) Z.-A. Qiao, L. Zhang, M. Guo, Y. Liu, Q. Huo, Synthesis of mesoporous silica nanoparticles via

- controlled hydrolysis and condensation of silicon alkoxide, *Chem.Mater.*, 2009, **21** (16), 3823-3829.
- (28) K. Suzuki, K. Ikari, H. Imai, Synthesis of mesoporous silica foams with hierarchical trimodal pore structures, *J. Am. Chem. Soc.*, 2003, **13** (7), 1812-1816.
- (29) Y. Chen, Q. H. Wang, T. M. Wang, One-pot synthesis of M (M = Ag, Au)@SiO<sub>2</sub> yolk-shell structures via an organosilane-assisted method: preparation, formation mechanism and application in heterogeneous catalysis, *Dalton trans.*, 2015, **44** (19), 8867-8875.
- (30) Y. Lu, Y. Mei, M. Drechsler, M. Ballauff, Thermosensitive core-shell particles as carriers for Ag nanoparticles: Modulating the catalytic activity by a phase transition in networks, *Angew. Chem.*, 2006, **45** (6), 813-816.